

Three-Dimensional Reconstruction of Weak-Lensing Mass Maps with a Sparsity Prior. II. Weighing Cluster

S. Yang¹★

¹Physics and Astronomy Department, Swarthmore College, Swarthmore, PA 19081

Received Month XX, YYYY; accepted Month XX, YYYY

ABSTRACT

In this thesis I will review some of basics in cosmology, gravitational lensing, dark matter halo profiles, and sparsity analysis. We will present some preliminary results in our attempt in 3D Mass map reconstruction.

Key words: gravitational lensing; weak; galaxies: clusters; general

1 INTRODUCTION

I will be following [Dodelson \(2003\)](#) and [Ryden \(2017\)](#) in this section where I cover some basics about cosmology and lensing by halos.

1.1 Basic Cosmology

We start with the Friedmann-Robertson-Walker (FRW) metric:

$$ds^2 = -c^2 dt^2 + a(t)^2 \left[\frac{dx^2}{1 - \kappa x^2/R_0^2} + x^2 d\Omega^2 \right] \quad (1)$$

where κ is the curvature in the universe which we will later take to be zero. We have in the standard cosmology model the Friedmann equation

$$\left(\frac{\dot{a}}{a}\right)^2 = \frac{8\pi G}{3c^2} \varepsilon - \frac{\kappa c^2}{R_0^2 a^2} \quad (2)$$

and the fluid equation

$$\dot{\varepsilon} + 3\frac{\dot{a}}{a}(\varepsilon + P) = 0 \quad (3)$$

and the equation of state

$$P = w\varepsilon. \quad (4)$$

We may also define

$$H(t) \equiv \frac{\dot{a}}{a} \quad (5)$$

and the critical density can be defined to be

$$\varepsilon_c(t) \equiv \frac{3c^2}{8\pi G} H(t)^2. \quad (6)$$

We also define the density parameter to be

$$\Omega(t) \equiv \frac{\varepsilon(t)}{\varepsilon_c(t)}. \quad (7)$$

★ syang3@swarthmore.edu

Ω_Λ refers to the density parameter of the cosmological constant or dark energy Ω_m being the density parameter of (cold) dark matter and baryonic matter, and Ω_r is the density parameter of radiations which includes mainly photon and neutrinos. In this work, we will assume the cosmology follows that of the Planck 2018 results and a flat universe, with $H_0 = 67.4 \text{ km s}^{-1} \text{ Mpc}^{-1}$, $\Omega_m = 0.315$, $\Omega_\Lambda = 0.685$ ([Planck Collaboration et al. 2020](#)).

1.2 Cluster Cosmology and Weak Lensing

Galaxy clusters, born from amplification of primordial perturbations, are the heaviest gravity-bounded objects in the Universe. The redshift evolution of abundance of galaxy clusters is sensitive to the growth rate of cosmic structures and expansion history of the Universe. By reconstructing the number of dark matter cluster at certain redshift with certain mass and comparing with halo mass function models (e.g. [Tinker et al. 2010](#)), we may constrain the underlying cosmological parameters including σ_8 and Ω_M . Clustering cosmology will also be a principal focus of upcoming galaxy surveys including *Euclid* and LSST (e.g., see [Laureijs et al. 2011](#) and [Ivezić et al. 2019](#)).

Gravitational lensing refers to the distortion of light from background galaxies due to foreground gravitational potentials. Neglecting the *B*-mode in lensing distortion (which is three orders of magnitudes smaller than *E*-mode, see [Krause & Hirata 2010](#)), this effect is usually described by 3 parameters, spin-0 convergence κ and two components of spin-2 shear $\gamma = \gamma_1 + i\gamma_2$, where convergence changes apparent galaxy sizes, and shear anisotropically distorts galaxy shapes. By measuring the coherent anisotropy in galaxy shapes, one can detect shear statistically.

Due to the ubiquitousness of this signal, one can measure it from every detected galaxy ([Li & Mandelbaum 2022](#)) at different positions and obtain a map of shear field. Then convergence map can be reconstructed using the shear map ([Kaiser & Squires 1993a](#)). This convergence map is also known as 2-D lensing mass map since it is the integrated foreground mass map along the line-of-sight (weighted by lensing kernel).

There are extensive studies on 2-D mass map reconstructed from weak gravitational lensing shear measurement, which focus on di-

rectly detecting galaxy clusters from weak lensing mass map without modeling the relation between optical observables and dark matter halo mass (Miyazaki et al. 2018; Hamana et al. 2020; Oguri et al. 2021). These studies detect clusters by finding peaks in the reconstructed 2-D mass map. However, 2-D lensing mass map does not provide redshift information of galaxy clusters. Therefore, we cannot use a 2-D mass map to directly study the *redshift evolution* of halo mass function.

This paper focuses on detecting and weighing galaxy clusters from 3-D mass map reconstructed from weak lensing shear measurements using the algorithm proposed by Li et al. (2021). The sparsity regularization — adaptive LASSO (Zou 2006) — utilized by our reconstruction should solve smearing problem of the reconstructed structures along the line of sight (Massey et al. 2007; Hu & Keeton 2002). We model the 3-D mass map as a sum of basis "atoms" in comoving coordinates as a given 3D density field. The basis "atoms" are constructed with NFW (Navarro et al. 1997) or cuspy NFW (Jing & Suto 2002) halos, which differs from other reconstruction schemes as GLIMPSE (Leonard et al. 2014) that our basis can account for the angular scale difference at different lens redshifts and is better suited to model clumpy mass distribution.

This paper is organized as follows: In Section ??, we introduce our algorithm for 3-D mass map reconstruction. In Section 4, we study the cluster detection and cluster mass, redshift estimation from 3-D mass map using one-halo simulations with different triaxial profiles. In Section 5, we study the performance of 3-D mass map reconstruction using two-halos simulations. In Section 6, we summarize and discuss the future application of the method to weak lensing imaging surveys.

2 MORE ON WEAK LENSING

2.1 Dark Matter Halo Profile

As the universe evolves in large scale according to Eqn. 2, some primordial perturbation results in a gravitational clustering of baryonic and dark matters. Such tightly bound structures are referred to as halos. We usually define the halo's radius with its mass enclosed in some radius r_{vir} such that

$$M_{\text{vir}} = \frac{4\pi}{3} r_{\text{vir}}^3 \Delta \rho_{\text{crit}}$$

where Δ is taken to be 200 in halo model proposed by Navarro et al. (1997). However, recent high resolution simulation has shown that halos tend to have universal mass profiles, exhibits triaxiality, and cuspy Navarro et al. (2010).

Following the definition of Jing & Suto (2002), we adopt a halo density profile of

$$\rho(R) = \frac{\delta_{\text{ce}} \rho_{\text{crit}}(z)}{(R/R_0)^\alpha (1 + R/R_0)^{3-\alpha}}, \quad (8)$$

where

$$R^2 \equiv c^2 \left(\frac{x^2}{a^2} + \frac{y^2}{b^2} + \frac{z^2}{c^2} \right) \quad (a \leq b \leq c). \quad (9)$$

Here, δ_{ce} is the concentration parameter of the halo. $\rho_{\text{crit}}(z)$ is the critical density of the universe at redshift z . R_0 is the scale radius of the triaxial halo. a , b and c are scaling factor that describes the shape of the halo.

From Eqn. (8), we see that the case of an isotropic halo model with $\alpha = 1$ reproduces the NFW halo profile. Various literature uphold different values of α ranging between $\alpha = 1$ and $\alpha = 1.5$ (see

e.g., Navarro et al. (1997), Moore et al. (1999), Oguri et al. (2003)). Therefore, we perform our subsequent analysis both on $\alpha = 1$ and $\alpha = 1.5$ cases.

JS02 also defines a length scale R_e such that $R_e/r_{\text{vir}} = 0.45$ Jing & Suto (2002) and the average density within an ellipsoid of R_e is

$$\Delta_e = 5 \Delta_{\text{vir}} \left(\frac{c^2}{ab} \right)^{0.75}, \quad (10)$$

where, from Oguri et al. (2001)

$$\Delta_{\text{vir}} = \frac{3M_{\text{vir}}}{4\pi r_{\text{vir}} \rho_{\text{crit}}} = 18\pi^2 (1 + 0.4093\omega_{\text{vir}}^{0.9052}) \quad (11)$$

if we have $\Omega_{m,0} + \Omega_{\Lambda,0} = 1$ and

$$\omega_{\text{vir}} = 1/\Omega_{\text{vir}} - 1, \quad (12)$$

and the density parameter Ω_{vir} at virialization is

$$\Omega_{\text{vir}} = \frac{\Omega_{m,0}(1 + z_{\text{vir}})^3}{\Omega_{m,0}(1 + z_{\text{vir}})^3 + (1 - \Omega_{m,0} - \Omega_{\Lambda,0})(1 + z_{\text{vir}}^2) + \Omega_{\Lambda,0}}. \quad (13)$$

Note that there is different definition for the concentration parameter $c \equiv \frac{r_{\text{vir}}}{R_0}$, where a numerical approximation is given as

$$c = A \cdot \left(\frac{M_{\text{vir}}}{10^{13} M_{\odot}} \right)^B \left(\frac{1.47}{1 + z} \right)^C \quad (14)$$

where $A = 6.02 \pm 0.04$, $B = -0.12 \pm 0.01$, and $C = 0.16 \pm 0.01$.

2.1.1 Convergence and Shear of Triaxial Halos

We align halo's major axis with the line of sight direction (for the most general case, see Oguri et al. (2003)), and define

$$\zeta = \frac{c^2}{b^2} x'^2 + \frac{c^2}{a^2} y'^2, \quad (15)$$

where the primed coordinate represent normalized observer's coordinate.

We therefore get an expression for the convergence κ as:

$$\begin{aligned} \kappa &= \frac{R_0}{\Sigma_{\text{crit}}} \int_{-\infty}^{\infty} \rho(R) dz' = \frac{R_0}{\Sigma_{\text{crit}}} \int_{-\infty}^{\infty} \frac{1}{\sqrt{f}} \rho \left(\sqrt{z_*'^2 + \zeta'} \right) dz'_* \\ &\equiv \frac{b_{\text{TNGF}}}{2} f_{\text{GNFW}}(\zeta). \end{aligned} \quad (16)$$

Here we have

$$f_{\text{GNFW}}(r) \equiv \int_0^{\infty} \frac{1}{\left(\sqrt{r^2 + z^2} \right)^\alpha \left(1 + \sqrt{r^2 + z^2} \right)^{3-\alpha}} dz. \quad (17)$$

Once we have an expression for κ , we may follow Keeton (2001) to calculate the shear field. Note that although in $\alpha = 1$ case an analytical solution can be yield, an analytical solution does not exist for a density profile with $\alpha = 1.5$. Note that, differing from Eqn. 4 in Li et al. (2021), we did not adopt truncation at a scale radius larger than the concentration parameter.

2.2 More Weak Lensing Basics

I will follow closely the review presented in Huterer (2010) and Mandelbaum (2018).

In newtonian gauge and natural units, the perturbed FRW metric can be written as

$$ds^2 = -(1 + 2\Psi)dt^2 + a^2(t)(1 - 2\Phi) \left[d\chi^2 + r^2 (d\theta^2 + \sin^2 \theta d\phi^2) \right], \quad (18)$$

where χ is the radial coordinate, θ and ϕ are angular coordinates, and a is the scale factor. $r(\chi)$ is the comoving distance and ϕ and ψ are the gravitational potentials. Weak lensing can be described as a linear transformation between unlensed (x_j, y_j) and lensed (x_i, y_i) coordinates as

$$\begin{bmatrix} x_j \\ y_j \end{bmatrix} = \begin{bmatrix} 1 - \gamma_1 - \kappa & -\gamma_2 \\ -\gamma_2 & 1 + \gamma_1 - \kappa \end{bmatrix} \begin{bmatrix} x_i \\ y_i \end{bmatrix} \quad (19)$$

The lensing shear is defined to be $\gamma = \gamma_1 + i\gamma_2$, which describes smearing of lense image due to gravitational potential. Note in the weak lensing limit we have $|\kappa|$ and $|\gamma| \ll 1$. The convergence κ results the change in shape and brightness of lensed objects. We may rewrite Eqn. 19 as

$$\begin{bmatrix} x_j \\ y_j \end{bmatrix} = (1 - \kappa) \begin{bmatrix} 1 - g_1 & -g_2 \\ -g_2 & 1 + g_1 \end{bmatrix} \begin{bmatrix} x_i \\ y_i \end{bmatrix} \quad (20)$$

where $g_i = \gamma_i/(1 - \kappa)$ is the reduced shear which is usually reconstructed in weak lensing measurements.

κ can be calculated formally by

$$\kappa(\mathbf{n}, \chi) = \int_0^\chi W(\chi') \delta(\chi') d\chi', \quad (21)$$

where $\delta = \frac{\rho - \bar{\rho}}{\bar{\rho}}$ is the relative perturbation in matter density and $W(\chi) = \frac{3}{2} \Omega_M H_0^2 g(\chi) (1 + z)$ is just a weight function. Ω_M is the matter energy density relative (baryonic and dark matter) to the critical density. H_0 is the Hubble constant in the present day universe. Also

$$g(\chi) = r(\chi) \int_\chi^\infty d\chi' n(\chi') \frac{r(\chi' - \chi)}{r(\chi')},$$

where $n(\chi)$ is the radial distribution of source galaxies.

By computing the projected potential using Ψ and Φ in Eqn. 18 with $\phi_{ij} = -(1/2) \int g(\chi) (\Psi_{ij} + \Phi_{ij}) d\chi$, we may calculate value for shear as

$$\gamma_1 = \frac{1}{2}(\psi_{11} - \psi_{22})$$

and

$$\gamma_2 = i\psi_{12}.$$

Here subscripts i, j means taking derivative in the x_i, x_j direction.

There is also a relationship between the κ field and γ field, derived in Kaiser & Squires (1993b):

$$\gamma(\mathbf{x}) = \frac{1}{\pi} \int_{\mathbb{R}^2} d^2 \mathbf{x}' \mathcal{D}(\mathbf{x} - \mathbf{x}') \kappa(\mathbf{x}') \quad (22)$$

where $\mathcal{D}(\mathbf{x}) = -(x - ix)^{-2}$ and \mathbf{x} is just the position in the sky.

We may also convert first acquire the fourier transform of $\tilde{\kappa}(\mathbf{k})$ and then using

$$\tilde{\gamma} = \pi^{-1} \mathcal{D}(\mathbf{k}) \tilde{\kappa}(\mathbf{k})$$

where

$$\tilde{\mathcal{D}}(\mathbf{k}) = \pi \frac{(k_1^2 - k_2^2 + 2ik_1 k_2)}{|\mathbf{k}|^2}$$

2.3 Weak Lensing in Operator Formulism

2.3.1 Model Dictionary

We incorporate our prior on density contrast field by modeling it as a sum of basis atoms in a ‘‘dictionary’’:

$$\delta = \mathbf{\Phi} \cdot \mathbf{x}, \quad (23)$$

where $\mathbf{\Phi}$ is the matrix operator transforming from the projection coefficient \mathbf{x} to the density contrast field δ . Its columns are the basis ‘‘atoms’’ of the model dictionary and denoted as $\phi_s(\mathbf{r}) = F_{\text{GNFW}}(\mathbf{r})\delta_D(z)$, where $\delta_D(z)$ is a Dirac δ function in the line-of-sight direction. One advantage of our model dictionary is that distinguish halos with similar mass at different redshift in terms of size in angular separation. An atom defined in the previous equation in angular separation coordinates is

$$\phi_s(\boldsymbol{\theta}, z) = \chi^2(z) F_{\text{GNFW}}(\boldsymbol{\theta} \mathbf{r}) \delta_D(z).$$

We then perform a convolution between projection coefficient vector with the dictionary to get the density contrast field

$$\delta(\mathbf{r}) = \sum_{s=1}^N \int d^3 r' \phi_s(\mathbf{r} - \mathbf{r}') x_s(\mathbf{r}').$$

From the density field, one can define the forward transform operator from the projection coefficient vector to the shear field as

$$\gamma = \mathbf{A} \cdot \mathbf{x} + \epsilon = \mathbf{P} \cdot \mathbf{Q} \cdot \mathbf{\Phi} \cdot \mathbf{x} + \epsilon,$$

where \mathbf{P} represents systematic effects and \mathbf{Q} represents the physical lensing effect.

2.3.2 Weak Lensing Operator

Again, the weak lensing operator can be conceived as a convolution process:

$$\mathbf{Q} = \int_0^{z_s} dz_l K(z_l, z_s) \int d^2 \theta \mathbf{D}(\boldsymbol{\theta} - \boldsymbol{\theta}'). \quad (24)$$

$K(z_l, z_s)$ is the lensing kernel between lens redshift z_l and source redshift z_s proposed by Bartelmann & Schneider (2001). It can be calculated using

$$K(z_l, z_s) = \begin{cases} \frac{3H_0\Omega_m}{2c} \frac{\chi(z_s)(1+z_l)}{\chi_s H(z_l)} / H_0 & (z_s > z_l) \\ 0 & (z_s \leq z_l) \end{cases} \quad (25)$$

$$\mathbf{D}(\boldsymbol{\theta}) = -\frac{1}{\pi}(\theta_1 - i\theta_2)^{-2}$$

is the Kaiser-Squires kernel Kaiser & Squires (1993b), which accounts for the angular separation between physical position of image source and gravitational potential source.

2.3.3 Systematics

The full systematics in our analysis involves uncertainty in redshift estimation, smoothing, and masking. Although in this work we did not consider the effect of redshift uncertainty.

The smoothing operator is defined as

$$\mathbf{W} = \int d^3 r' W(\mathbf{r} - \mathbf{r}'),$$

where

$$W(\boldsymbol{\theta}, z) = W_t(\boldsymbol{\theta}) W_l(z),$$

where

$$W_i(\theta) = \frac{1}{2\pi\beta^2} \exp\left(-\frac{|\theta|}{2\beta^2}\right)$$

and

$$W_l(z) = \begin{cases} 1/\Delta z & (|z| < \Delta z/2) \\ 0 & \text{otherwise} \end{cases}.$$

We have set $\beta = 0$ (the smoothing scale) in this case, corresponding to no smoothing.

We also have to account for the effect of Masking, which is simply described as

$$\mathbf{M} = \int d^3 r' M(\mathbf{r}' \delta_D(\mathbf{r} - \mathbf{r}')) \quad (26)$$

where

$$M(\mathbf{r}) = \begin{cases} 1 & n_{\text{sm}} \geq 1 \\ 0 & \text{otherwise} \end{cases}$$

which just selects out positions where a galaxy can be detected.

So the systematic operator is $\mathbf{P} = \mathbf{M} \cdot \mathbf{W}$

2.3.4 Normalization

Finally, we note that we also will weight columns of \mathbf{A} by the inverse of the noise covariance matrix. So the l^2 norm of i th column of \mathbf{A} is

$$N_i = (\Sigma^{-1})_{\alpha\beta} A_{i\alpha} A_{i\beta}$$

and the normalized forward transform matrix and project parameters are given by

$$\begin{aligned} A'_{\alpha\beta} &= A_{\alpha\beta} / N_{\alpha}^{\frac{1}{2}} \\ x'_{\beta} &= x_{\beta} N_{\beta}^{\frac{1}{2}} \end{aligned}$$

3 SPARSITY ANALYSIS

We will follow the standard introduction to this subject presented in [Hastie et al. \(2015\)](#) as we introduce the basics of sparsity analysis. Given the prevalence and the strength of noise in weak lensing analysis, to successfully reconstruct physical information from weak lensing data, one may be prompted to use *sparsity*. A *sparse* model indicates only a relatively small amount of parameters controls the behavior of the system. In weak lensing and specifically 3D reconstruction, we apply this idea to assert that galaxy clusters are only sparsely distributed in the present universe.

To implement the sparsity prior in an analysis, first consider the familiar linear regression model:

$$y_i = \beta_0 + \sum_{j=1}^p x_{ij} \beta_j + e_i \quad (27)$$

where β_0 and $\beta = (\beta_1, \beta_2, \dots, \beta_p)$ are unknown multidimensional linear parameters of some model. y_i 's are measured values, and e_i 's are errors of estimation.

To retrieve the best predicted model, one acquire an estimation of β parameters by minimizing the least-squares objective function.

$$\text{minimize}_{\beta, \beta_0} \sum_{i=1}^N (y_i - \beta_0 - \sum_{j=1}^p x_{ij} \beta_j)^2 \quad (28)$$

However, when the number of undertermined parameters is large, such an objective function may yield nonzero value for the β vector and yield degenerate solutions. This makes the interpretation of the result difficult. A solution is just to *regularize* the estimation process. The regime we will be working with in this work is called the Lasso regularization, which uses the Lasso Estimator:

$$\text{minimize}_{\beta_0, \beta} \left\{ \frac{1}{2N} \sum_{i=1}^N (y_i - \beta_0 - \sum_{j=1}^p x_{ij} \beta_j)^2 \right\} \quad (29)$$

subject to

$$\|\beta\|_1 \leq t.$$

Where $\|\beta\|_1$ represents the l_1 -norm which is the sum of the absolute values of each entries in β .

In matrix form, one may have

$$\text{minimize}_{\beta_0, \beta} \left\{ \frac{1}{2N} \|\mathbf{y} - \beta_0 \mathbf{1} - \mathbf{X}\beta\|_2^2 \right\} \quad (30)$$

subject to

$$\|\beta\|_1 \leq t.$$

One can also rewrite this into the Lagrangian form

$$\text{minimize}_{\beta \in \mathbb{R}^p} \left\{ \frac{1}{2N} \|\mathbf{y} - \mathbf{X}\beta\|_2^2 + \lambda \|\beta\|_1 \right\} \quad (31)$$

Here then $\lambda \geq 0$ now controls the degree of sparsity we impose on the minimization, with larger λ correspond to stronger sparse condition.

3.1 Adaptive Lasso Regression

However, it is found that when the column vectors are strongly correlated in Eqn. 31, the traditional Lasso regression loses its oracle properties [Zou \(2006\)](#). In our application, this is due to the strongly correlated form of weak lensing kernels [Li et al. \(2021\)](#). The adaptive Lasso regression proposed in [Zou \(2006\)](#) is proven to solve this problem.

First, we acquire an estimator from the “traditional” Lasso regression algorithm using

$$\hat{x}^{\text{LASSO}} = \arg \min_x \left\{ \frac{1}{2} \sum \|(\gamma - \mathbf{A}' \cdot x')\|_2^2 + \lambda \|x'\|_1 \right\}. \quad (32)$$

Then, we use the adaptive weight \hat{w} ,

$$\hat{w} = \frac{1}{|\hat{x}'_{\text{LASSO}}|^\tau}, \quad (33)$$

to penalize different projection coefficient in the l^1 penalty. In our analysis τ is set to 2.

Finally, we acquire the adaptive Lasso estimator with

$$\hat{x}' = \arg \min_{x'} \left\{ \frac{1}{2} \sum \|(\gamma - \mathbf{A}' \cdot x')\|_2^2 + \lambda \|\hat{w} \circ x'\|_1 \right\}, \quad (34)$$

where the same value for λ is used to acquire the Lasso estimator. “ \circ ” refers to the element-wise dot product. The philosophy of the adaptive Lasso regression is to further shrink down coefficients with smaller amplitudes.

4 ONE HALO

In this section we test the mass map reconstruction on one-halo simulations of general triaxial halos. In Section ??, we present the density profile and lensing effects of triaxial halos; in Section 4.1, we describe the triaxial halo simulations used to test our mass mapping algorithm; in Section 4.2, we show the results on noiseless simulations; in Section 4.3, we show the results on noisy simulations;

4.1 Simulation setup

4.1.1 from halo properties to lensing shear

In this section, we introduce our simulation used to test the mass map reconstruction and quantify biases in the halo mass and redshift estimations.

In our simulations, we use halos with different triaxial shapes, with ellipticity, defined as $\frac{a}{c}$, ranging from 1 to 0.5. However, to reduce the dimensionality in our dictionary space in the reconstruction, the dictionaries are prepared with isotropic halos with $a = b = c$ described in the previous section. The redshifts of simulated halos range from $z = 0.1$ to $z = 0.5$.

To include a more diverse halo profile as shown in various high-resolution N -body simulations (Navarro et al. 2010), we include the ability to simulate triaxial halos (Jing & Suto 2002) with both (i) the NFW (Navarro et al. 1997) radial profile and (ii) the cuspy NFW radial profile Jing & Suto (2000).

Unlike Li et al. (2021) which adopted analytical NFW halo dictionaries, for more flexibility in our algorithm to incorporate shear field produced by different (potentially anisotropic) halo models (for which a closed-form solution may not exist), we investigated simulation by preparing numerical “dictionaries”. They are generated by the following steps:

- (i) Indicating the type of halo from which a dictionary desires to be built. Note that a set of dictionary may contain a mixture halo models, see (chapter on mixed model)
- (ii) Indicating the virialized mass of the halo.
- (iii) Indicating either the concentration parameter or the scale radius of the halo. The mass and one of these two parameters are sufficient to determine the shear field for either NFW or the cuspy NFW halo.
- (iv) Generate $2000N$ sample points for a reconstruction of shear field with N pixels and use either Eqn. 16 and Kaiser-Squire transformation
- (v) Use Eqn. 16 and Kaiser-Squire transformation to acquire the noiseless smoothed underlying shear field produced by the halo specified by the above parameters.

For noiseless simulation, we generated in total of $2000 \times 48 \times 48$ galaxies with shear signal described in this section in a 48×48 pixelized grid covering $98\text{arcmin} \times 98\text{arcmin}$ of sky area. We sample 5 halo masses ranging from $10^{14.4}h^{-1}M_{\odot}$ to $10^{15.2}h^{-1}M_{\odot}$ in our simulation, and for each halo mass, 100 halos are sampled linearly from $z = 0.0625$ to $z = 0.4675$ and from $\frac{a}{c} = 1$ to $\frac{a}{c} = 0.5$.

4.1.2 Observational Noise

For noisy simulation, we adopt noise, including galaxy shape noise and measurement error, calculated using the first-year shear catalog of the Subaru Hyper Suprime-Cam (Mandelbaum et al. 2017). We

utilized the formulation of Shirasaki et al. (2019), where we have

$$e^{\text{int}} = \left(\frac{e_{\text{rms}}}{\sqrt{e_{\text{rms}}^2 + \sigma_e^2}} \right) e^{\text{ran}}, \quad e^{\text{mea}} = N_1 + i N_2,$$

where e^{int} represents the per-component intrinsic shape error, and e^{mea} represents the per-component shape measurement error. $e^{\text{ran}} = e^{\text{obs}} e^{i\phi}$. $e^{i\phi}$ serves to rotate the observed shape, $e^{\text{obs}} = e_1^{\text{obs}} + i e_2^{\text{obs}}$, by some random angle ϕ . N_1, N_2 are random numbers drawn from a Gaussian centered at 0 with a standard deviation of σ_e . e_{rms} is the root-mean-square of the intrinsic galaxy shape for each shape component. σ_e is the standard deviation of the shape measurement error due to image noise for each shape component. Note, e_{rms} and σ_e are estimated from image simulations at single galaxy level using realistic galaxy image simulations (Mandelbaum et al. 2018).

We also have an expression for the observed shear:

$$\gamma^{(\text{obs})} = \frac{1}{1 + \langle m \rangle} \left(\frac{e}{2\mathcal{R}} - c \right). \quad (35)$$

where $\langle m \rangle$, the weighted average of multiplicative bias, was set to zero and $\mathcal{R} = 1 - \langle e_{\text{rms}}^2 \rangle$. We can then substitute

$$e = e^{\text{ran}} + e^{\text{mea}}$$

to get a mock shear field.

The noisy simulation then proceed with generating $8 \times 48 \times 48$ galaxies with shear signal described in this section in a 48×48 pixelized grid covering $98\text{arcmin} \times 98\text{arcmin}$ of sky area. This is equivalent to generating detecting 20 galaxies per arcminute squared. 100 halos are sampled linearly from $z = 0.0625$ to $z = 0.4675$ and from $\frac{a}{c} = 1$ to $\frac{a}{c} = 0.5$. For each set of halo parameter (z and $\frac{a}{c}$) We then initiate our adaptive LASSO regression using the FISTA algorithm for 150000 iterations. We will then record average mass and redshift of the reconstructed halo, as well as the percentage of correct redshift estimation.

We adopt a much smaller number of galaxies on a grid than the noiseless simulation case because we wish recreate a realistic galaxy number density close to most lensing surveys (cite some lensing survey about galaxy number) in the noisy case but were just verifying the algorithm in the noiseless simulation.

4.2 Noiseless Reconstruction

In this section we present reconstruction results for triaxial NFW and cuspy NFW halos with numerical frames. In Figure (insert fig number) and Figure (insert figure name), the mass bias (defined to be the different between real mass and the reconstructed mass over true mass) and redshift estimate bias were shown for 2 types of halo (NFW and cuspy NFW halo) reconstructed using numerical dictionary with the same parameter (M_{vir} , concentration parameter, etc.). We performed 100 reconstruction across different z and $\frac{a}{c}$ with $\lambda = 2$ and $M_{\text{vir}} = 10^{14.6}M_{\odot}$, $10^{14.8}M_{\odot}$, and $10^{15.0}M_{\odot}$.

A sample reconstruction result looks like the following:

4.3 Noisy Reconstruction

4.4 λ Determination

To determine the parameter λ_{ada} in Eqn. 29 in (Li et al. 2021) that optimizes reconstruction results, we perform various single halo reconstruction of shear field produced by an isotropic halo of mass $10^{14.6}, 10^{14.8}, 10^{15.0}$, and $10^{15.4} M_{\odot}$ at an intermediate redshift ($z = 0.2425$) from 500 iterations. Examining the density plot for small λ and large λ , for each cases we observe that a small λ parameter will results in detection with an underestimation of masses, probably due to a failure of sparsity constraint, as indicated by the long tail of small mass reconstructions. We may also conclude that a relatively higher λ should better enforce the sparsity condition, while effective making a cutoff for small mass detection. Also, there is no clear “best” value for λ , as there is a trade off between detection rate and mass bias estimation. From some of our later results, it is also evident that the best value of λ depends on both the mass and the redshift of the halo. From this, we conclude that we should find an optimized λ for interval targeted detection mass, and then recursively apply SPLINV to detect galaxy halo in each mass interval.

4.5 Mass Estimation

In this section we present reconstruction results for triaxial NFW and cuspy NFW halos with numerical frames. In Fig. ?? to and Fig. ??, we present the reconstructed(measured) mass for the 2 types of halo with ellipticity $\frac{a}{c}$ ranging from 1 to 0.5 reconstructed using numerical dictionary with the same M_{vir} and concentration parameter, but with $\frac{a}{c} = 1$ (isotropic). We performed 500 used noise simulation setup described in ?? to perform reconstruction across different z and $\frac{a}{c}$ with 500 realizations with $\lambda = 2$, which targets halo with relatively smaller mass, for each value of $\frac{a}{c}$ and z and 100 realizations with $\lambda = 4$ and $\lambda = 4$, which targets halo with higher masses. At lower redshifts, corresponding to stronger lensing signal, the choice of $\lambda = 2$ gives exquisite halo mass estimations. Observing panel (a) in Fig. ?? and Fig. 7, we conclude that a large λ value may result in a systematic overestimation of the halo masses, probably due to the fact that only the strongest lensing signal are detected during the reconstruction. However, the non-monotonous pattern in panel (b) of Fig. ?? and Fig. 7 indicates that one might could optimize the value of λ for each halo at each redshift. We may also see that for reconstruction of more massive halos results in an underestimation of masses. This could be caused by the fact that a smaller λ enforces a weaker sparsity condition and SPLINV may confuse the large signal due to the massive halo as signal generated by two separate halos. Another trend we may conclude is that, the smaller cuspy halos are generally harder to detect and hence will tend to have larger detection bias.

Fig. ?? and Fig. ?? shows the mass estimation of halos of masses $10^{14.8}, 10^{15.0}, 10^{15.2}$ and $10^{15.4} M_{\odot}$. We observe in panel (a) of these two plots that, while detection for smaller mass halo at lower redshift with a big λ yields good mass estimation and high detection rate (as seen from the small error bar), the performance of SPLINV decreases drastically as redshift of the halo increases. With a larger λ , we see that the mass estimation for larger mass improves, with performance of reconstructing NFW halos better than that of cuspy NFW halos.

4.6 Redshift Estimation

Here we represent results of redshift estimate from simulations described in Sect. ?. We first note that the slight overestimation of

redshift in panel (b), (c), and (d) in Fig. 8 and 9 is due to the discrete nature of possible redshift bins, where there is no option for an underestimation halo lower redshift halos. Other than this, we may observe that the redshift estimation is consistently accurate, with no significant dependence on the shape ($\frac{a}{c}$ value) of the halo.

4.7 Systematic Error in Dictionary

In this section we present the effect of where the dictionary does not match the underlying halo producing the halo. We argue that using the assumption that the underlying halo of the universe is isotropic NFW halos we can still detect accurately the redshift and masses of galaxy clusters. To do this, we examined for (1) the effect of erroneous assumption of halo dictionary and (2) the effect of rotation in the θ angle on single halo reconstruction.

Comparing Fig. 12 and Fig. 4, we see that although the results in Fig. 12 uses the “wrong” dictionary (the shear field is produced by a cuspy NFW halo but the dictionary uses NFW halo), the reconstructed result still resembles that in Fig. 4.

Also comparing Fig. 14 with the first panel of 4, we again see good agreement with reconstruction using isotropic halo model and we rotate a highly anisotropic halo with $\frac{a}{c} = 0.5$ in the polar direction for $\theta = 30^\circ, 60^\circ, 90^\circ$. The results from this section and the previous one indicate that, even when the true halo that constitutes the κ map of the universe may be anisotropic, one may still recover the underlying mass map using isotropic models.

5 TWO HALOS

In this section we test our algorithm under the conditions with (1) 2 halos with smaller and smaller distance on the sky and (2) Our numerical dictionary contains multiple halo models.

5.1 Two-halo Simulations

We start our series of simulation with two halos (1) at a same medium redshift $z = 0.2425$ or (2) at two different redshifts....

We then decrease the distance between the two halos on the grid (as measured by ra and dec) by linear intervals, and perform the simulation again until the simulation “fails”, where fail would mean either (1) the number of halo detected is wrong or (2) the redshift estimate of a halo is wrong.

Other aspects of the simulation is identical to ?.

This simulation setup is design to determine the limit of sparsity linear inversion at distinguishing distinct halos.

5.1.1 Noiseless Two Halo Simulation

We also performed an analysis of reconstruction resolution, where we detect mass estimation bias of two halos in proximity. We simulated two isotropic NFW halo of mass $10^{14.8} M_{\odot}$ at the same redshift of $z = 0.2425$, from distance 2400 arcsec to 0 arcmin. This result is shown in Fig. 15. Observe that until the borderline of 240 arcsec, the mass estimation of the two halos are very accurate. Hence, we expect significant mass bias due to nearby halos in noisy reconstructions, where signals of two adjacent halo combined with noise together creates a shear estimation that resembles a different halo (false detection) which affects the mass and redshift estimation of the originally halo. This is a motivation that, in a realistic reconstruction of noisy shear map, we should first use a large λ value to

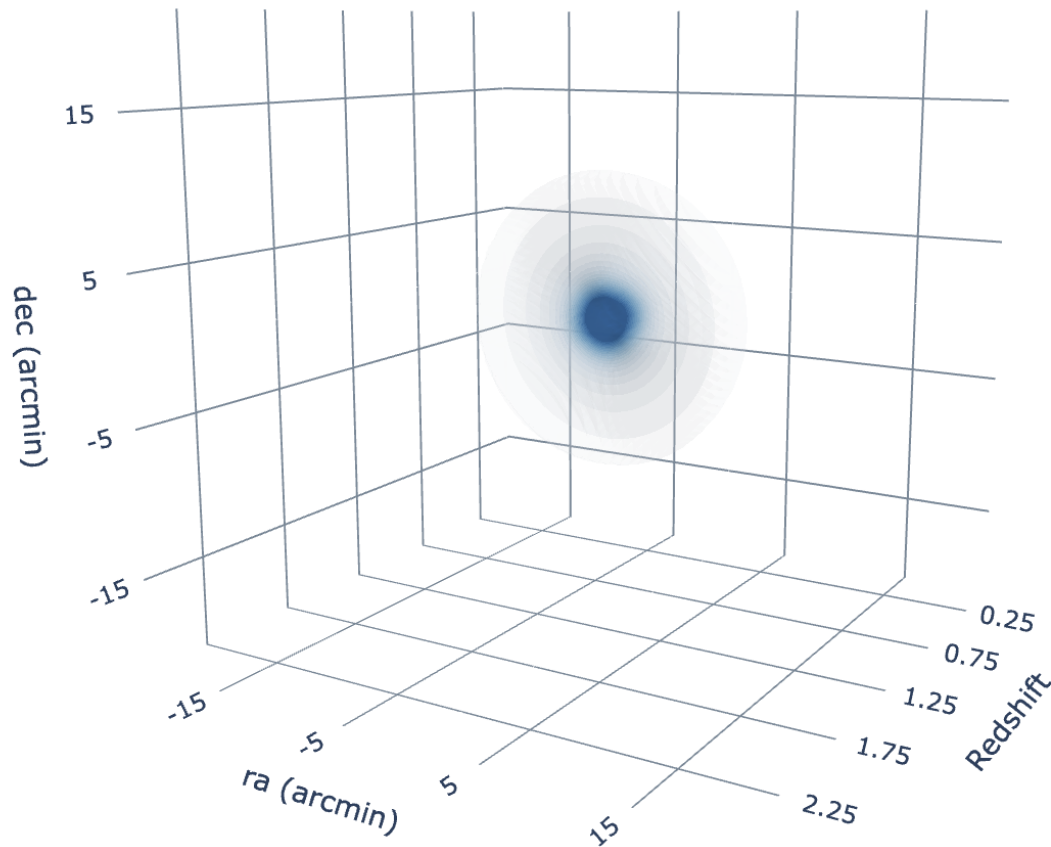


Figure 1. A Sample Plot of Reconstruction Result

detect massive halos and subtract signals from these halos to avoid false detection.

5.2 Resolution limit

In this section, we used two halos with the same mass of $M = 10^{14.8} M_{\odot}$. Starting 2400 arcsec apart at the same redshift of $z = 0.2425$ and gradually decreasing their distance to 0 arcsec (overlapping halos). We present the sum of the two reconstructed mass in Fig. . We see that, in the noiseless case, our simulation method demonstrate exquisite resolution until 300 arcsec.

5.3 Mass and Redshift Estimations

6 SUMMARY

ACKNOWLEDGEMENTS

DATA AVAILABILITY

The code used for mass map simulation and reconstruction in this paper is available from <https://github.com/mr-superonion/splinv>.

REFERENCES

- Bartelmann M., Schneider P., 2001, *Physics Reports*, 340, 291
Dodelson S., 2003, *Modern Cosmology*. Academic Press, San Diego, CA
Hamana T., Shirasaki M., Lin Y.-T., 2020, *PASJ*, 72, 78
Hastie T., Tibshirani R., Wainwright M., 2015, *Statistical learning with sparsity*. Chapman & Hall/CRC Monographs on Statistics and Applied Probability, Productivity Press, New York, NY
Hu W., Keeton C. R., 2002, *Physical Review D*, 66
Huterer D., 2010, *J* 10.1007/s10714-010-1051-z
Ivezić Ž., et al., 2019, *ApJ*, 873, 111
Jing Y. P., Suto Y., 2000, *ApJ*, 529, L69
Jing Y. P., Suto Y., 2002, *The Astrophysical Journal*, 574, 538
Kaiser N., Squires G., 1993a, *ApJ*, 404, 441
Kaiser N., Squires G., 1993b, *The Astrophysical Journal*, 404, 441
Keeton C. R., 2001, A Catalog of Mass Models for Gravitational Lensing, [doi:10.48550/ARXIV.ASTRO-PH/0102341](https://arxiv.org/abs/astro-ph/0102341), <https://arxiv.org/abs/astro-ph/0102341>
Krause E., Hirata C. M., 2010, *A&A*, 523, A28
Laureijs R., et al., 2011, Euclid Definition Study Report, [doi:10.48550/ARXIV.1110.3193](https://arxiv.org/abs/1110.3193), <https://arxiv.org/abs/1110.3193>
Leonard A., Lanusse F., Starck J.-L., 2014, *MNRAS*, 440, 1281
Li X., Mandelbaum R., 2022, arXiv e-prints, p. arXiv:2208.10522
Li X., Yoshida N., Oguri M., Ikeda S., Luo W., 2021, *ApJ*, 916, 67
Mandelbaum R., 2018, *Annual Review of Astronomy and Astrophysics*, 56,

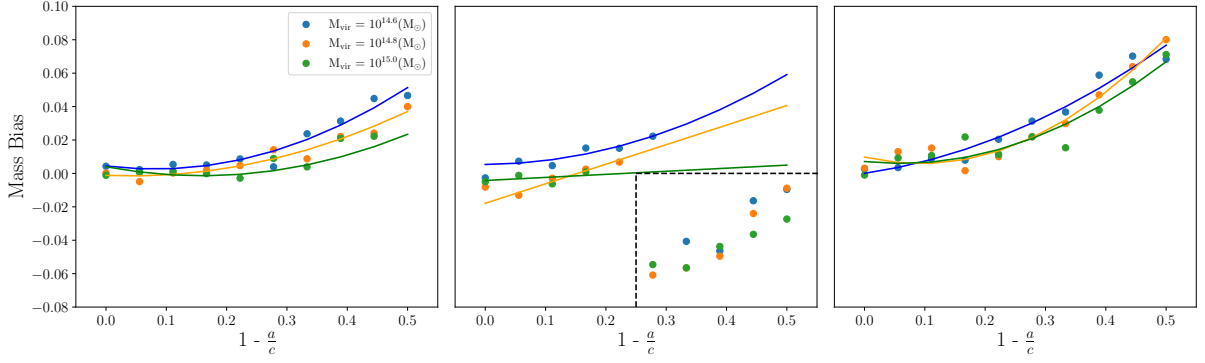


Figure 2. Noiseless reconstruction results for NFW halo with $M = 10^{14.6}, 10^{14.8}, 10^{15.0} M_{\odot}$ using $\lambda = 2$. The dots represent reconstruction results and the solid curves are second order polynomial approximation to the data. The data points enclosed by the black dashed line correspond to an overestimation of redshifts, which is probably due to the fact that the triaxial halo appears smaller with a smaller value of $\frac{a}{c}$.

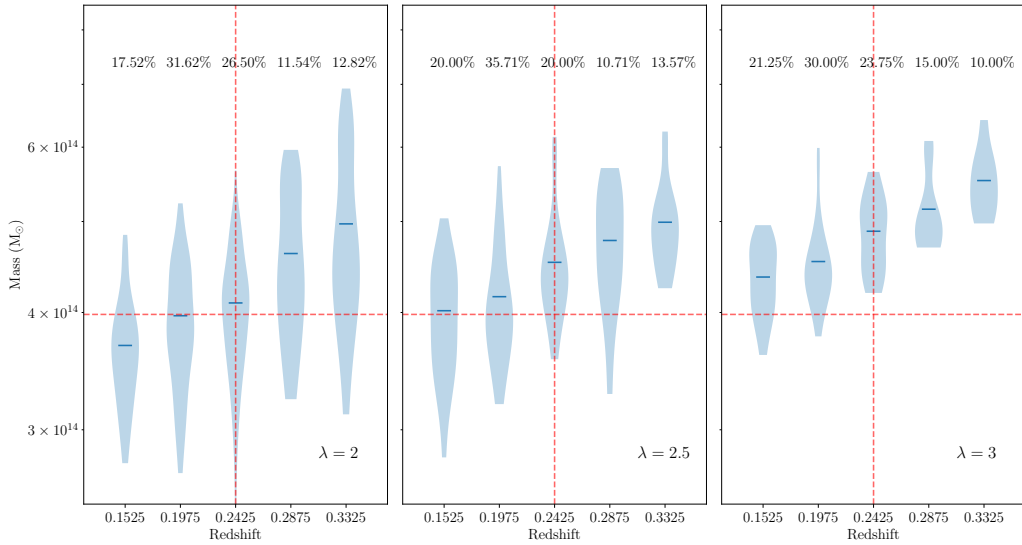


Figure 3. Detection number density plot of halo with mass $10^{14.6} M_{\odot}$. The blue shaded area indicate the number density of detected mass that correspond to the indicated mass and redshift. The true detection probabilities are 47%, 28%, and 16% for each value of λ .

393
Mandelbaum R., et al., 2017, *Publications of the Astronomical Society of Japan*, 70
Mandelbaum R., et al., 2018, *MNRAS*, 481, 3170
Massey R., et al., 2007, *at*, 445, 286
Miyazaki S., et al., 2018, *PASJ*, 70, S27
Moore B., Ghigna S., Governato F., Lake G., Quinn T., Stadel J., Tozzi P., 1999, *The Astrophysical Journal*, 524, L19
Navarro J. F., Frenk C. S., White S. D. M., 1997, *The Astrophysical Journal*, 490, 493
Navarro J. F., et al., 2010, *Monthly Notices of the Royal Astronomical Society*, 402, 21
Oguri M., Taruya A., Suto Y., 2001, *The Astrophysical Journal*, 559, 572
Oguri M., Lee J., Suto Y., 2003, *The Astrophysical Journal*, 599, 7
Oguri M., et al., 2021, *PASJ*, 73, 817
Planck Collaboration et al., 2020, *ApJ*, 641, A6

Ryden B., 2017, *Introduction to cosmology*. Cambridge University Press, Cambridge, England
Shirasaki M., Hamana T., Takada M., Takahashi R., Miyatake H., 2019, *Monthly Notices of the Royal Astronomical Society*, 486, 52
Tinker J. L., Robertson B. E., Kravtsov A. V., Klypin A., Warren M. S., Yepes G., Gottlöber S., 2010, *The Astrophysical Journal*, 724, 878
Zou H., 2006, *Journal of the American Statistical Association*, 101, 1418

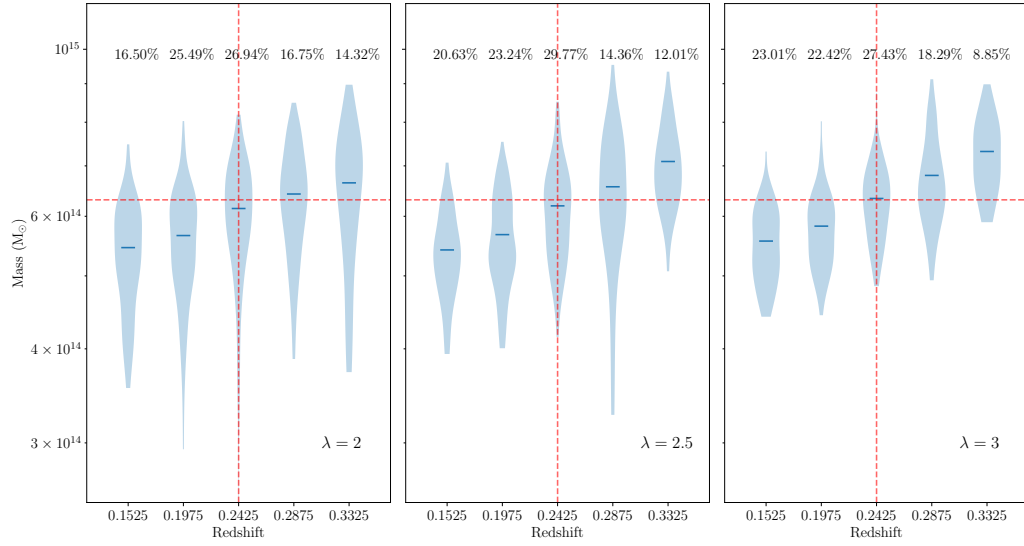


Figure 4. Detection number density plot of halo with mass $10^{14.8} M_{\odot}$. The blue shaded area indicate the number density of detected mass that correspond to the indicated mass and redshift. The true detection probabilities are 82%, 77%, and 68% for each value of λ respectively.

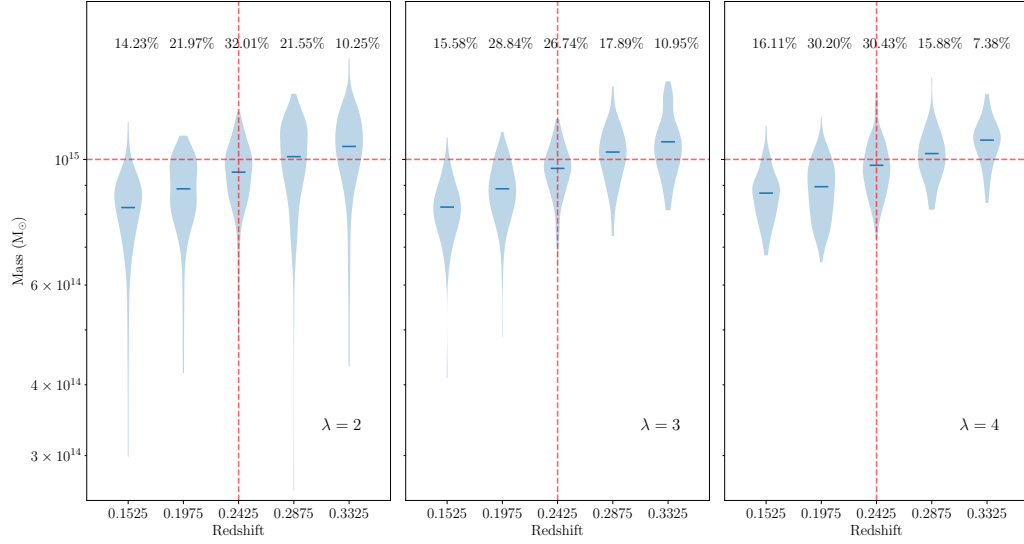


Figure 5. Detection number density plot of halo with mass $10^{15.0} M_{\odot}$. The blue shaded area indicate the number density of detected mass that correspond to the indicated mass and redshift. The true detection probabilities are 89%, 95%, and 95% for each value of λ .

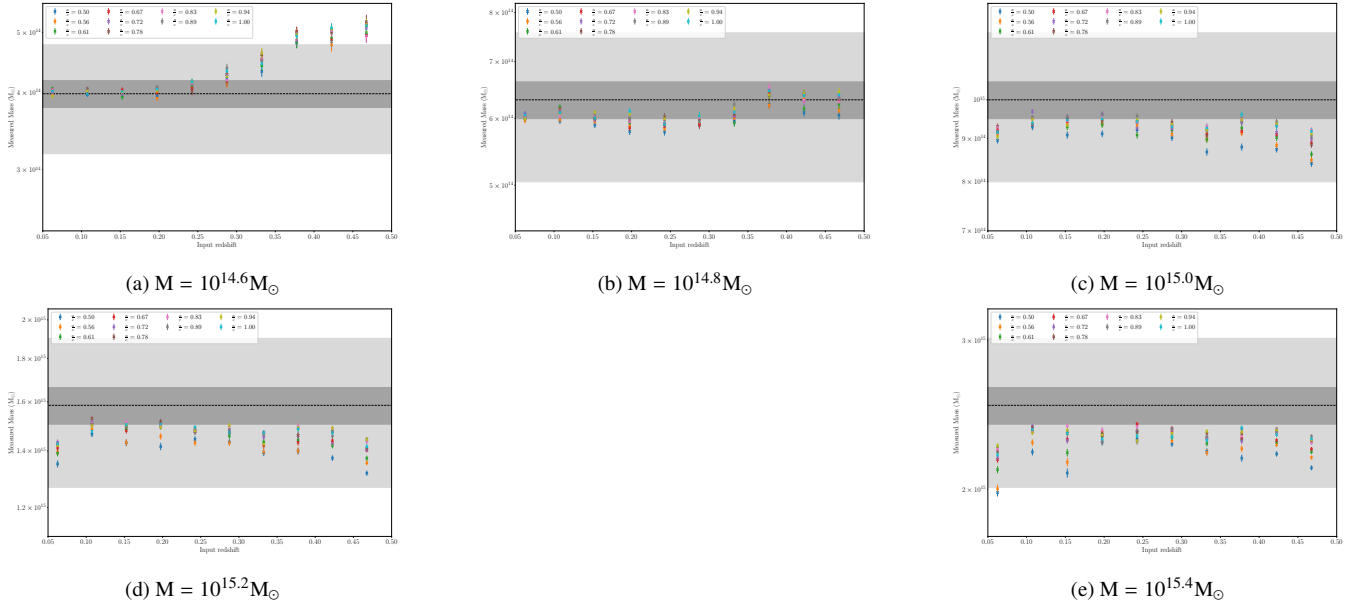


Figure 6. NFW halo Mass Bias for $M = 10^{14.6}, 10^{14.8}, 10^{15.0}, 10^{15.2}$ and $10^{15.4} M_{\odot}$ respectively, reconstructed using $\lambda = 2$. The darker grey area indicate a 5% bias and the lighter grey area indicate a 20% mass bias.

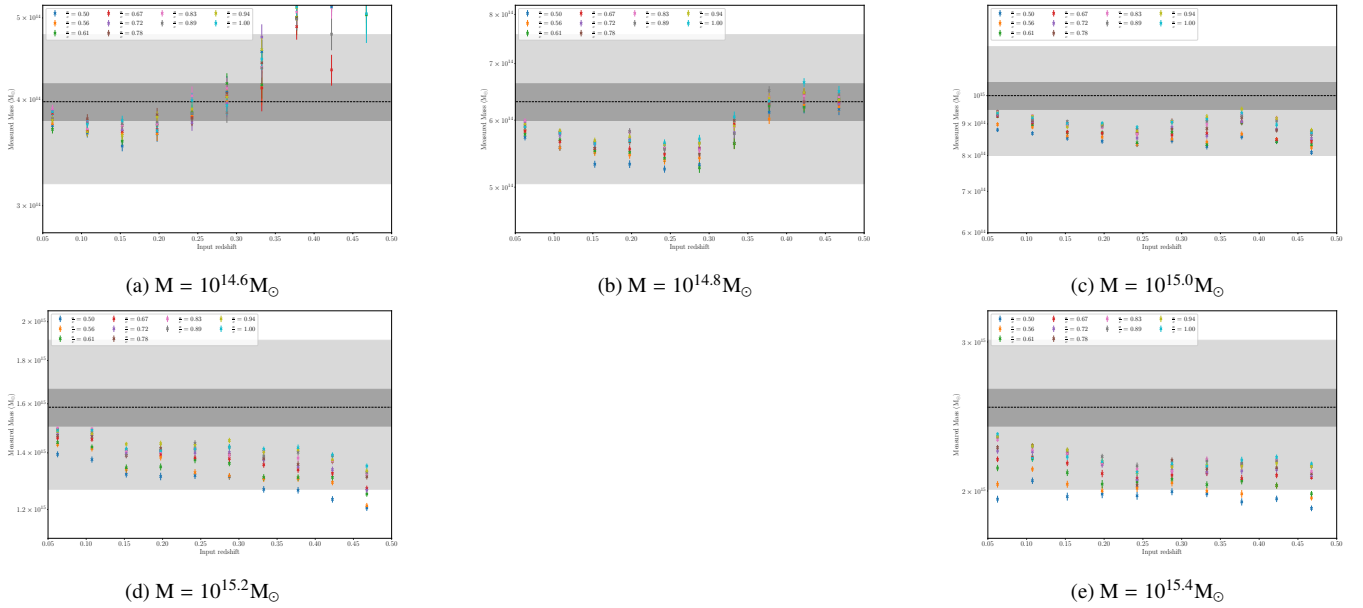


Figure 7. Cuspy NFW halo Mass Bias for $M = 10^{14.6}, 10^{14.8}, 10^{15.0}, 10^{15.2}$ and $10^{15.4} M_{\odot}$ respectively, reconstructed using $\lambda = 2$. The darker grey area indicate a 5% bias and the lighter grey area indicate a 20% mass bias.

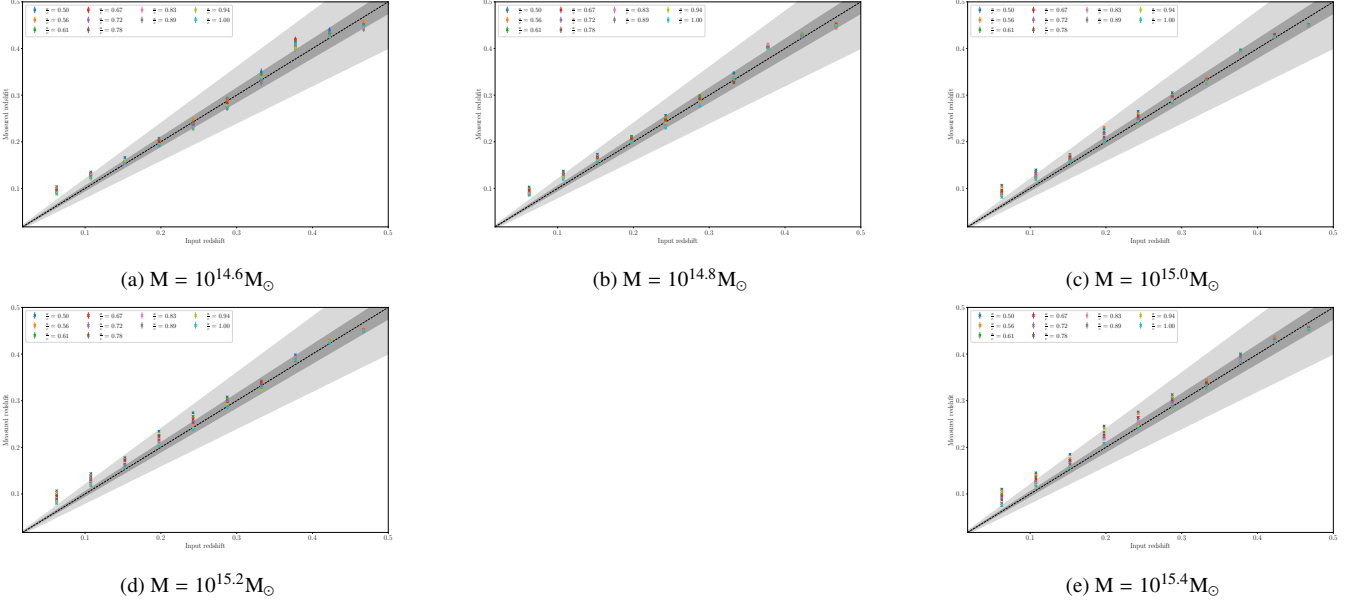


Figure 8. NFW halo Redshift Estimation for $M = 10^{14.6}, 10^{14.8}, 10^{15.0}, 10^{15.2}$ and $10^{15.4} M_{\odot}$ respectively, reconstructed using $\lambda = 2$. The darker grey area indicate a 5% bias and the lighter grey area indicate a 20% mass bias.

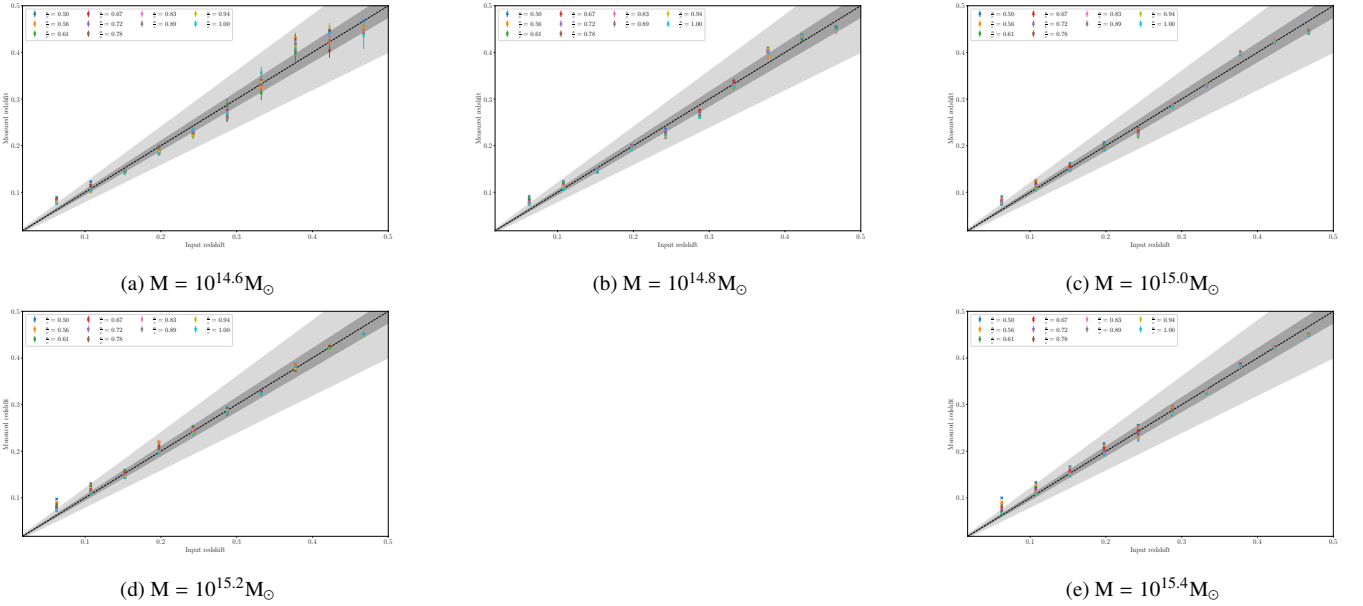


Figure 9. Cuspy NFW halo Redshift Estimation for $M = 10^{14.6}, 10^{14.8}, 10^{15.0}, 10^{15.2}$ and $10^{15.4} M_{\odot}$ respectively, reconstructed using $\lambda = 2$. The darker grey area indicate a 5% bias and the lighter grey area indicate a 20% mass bias.

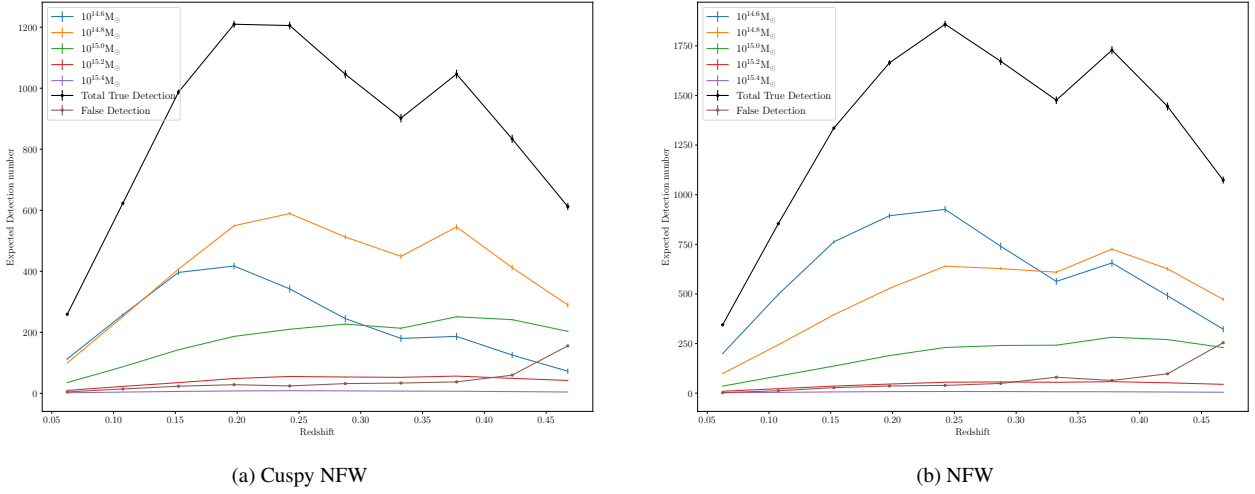


Figure 10. Left:

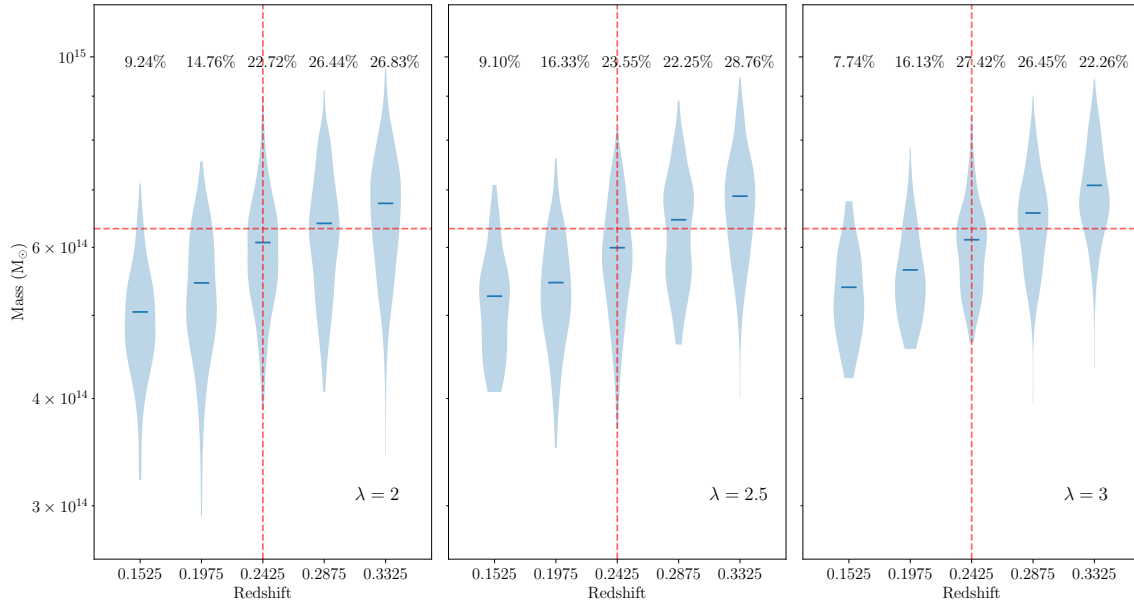


Figure 11. Detection number density plot of cuspy NFW halo with mass $10^{14.8} M_{\odot}$. The blue shaded area indicate the number density of detected mass that correspond to the indicated mass and redshift. The true detection probabilities are 78%, 69%, and 62% for each value of λ respectively.

Figure 12. Left:

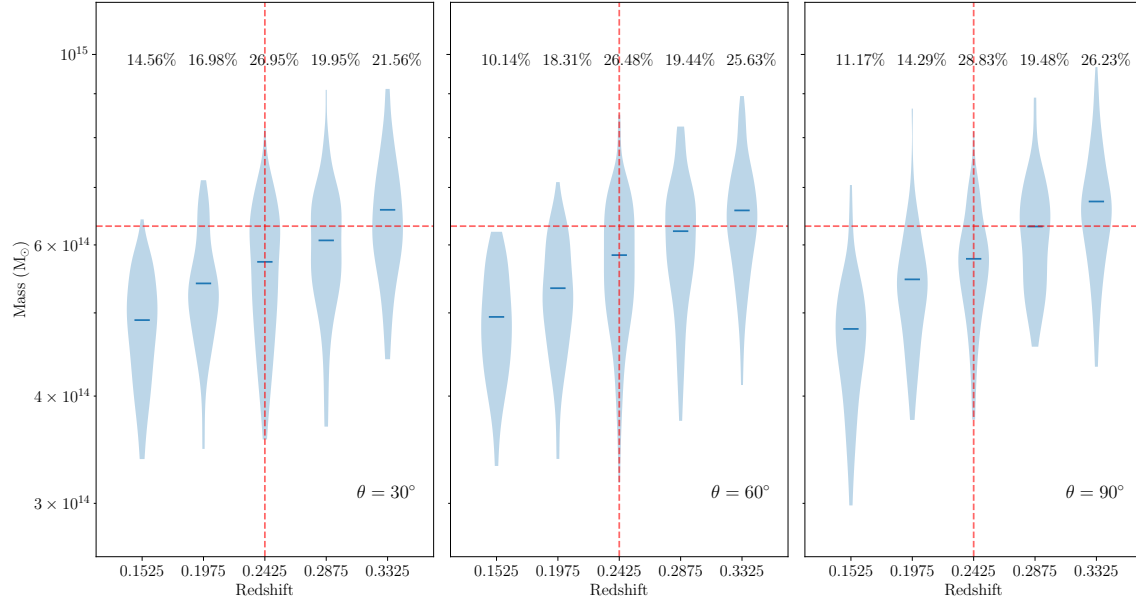


Figure 13. Detection number density plot of NFW halo with $\frac{a}{c} = 0.5$ with mass $10^{14.8} M_\odot$, but with $\theta = 30^\circ, 60^\circ, 90^\circ$. The blue shaded area indicate the number density of detected mass that correspond to the indicated mass and redshift. The true detection probabilities are 74%, 71%, and 77% for each value of λ respectively.

Figure 14. Left:

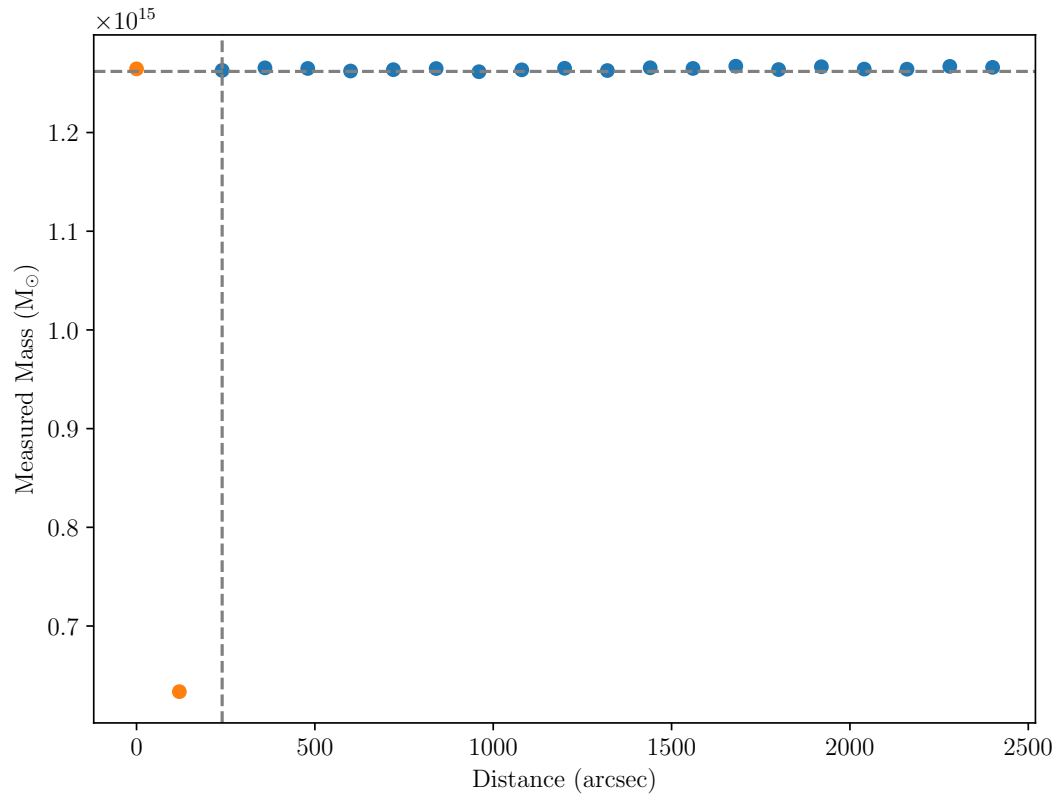


Figure 15. Total mass estimation for a noiseless two halo simulation. The vertical grey dashed indicates the cutoff where two adjacent halo getting reconstructed as a single halo. The horizontal grey line indicates the true value of total mass.